# Catalytic photo-redox of simulated air into ammonia over bimetallic MOFs nanosheets with oxygen vacancies

Wenjun Zhao [a], Jiangzhou Qin [b], Wei Teng [c], Jincheng Mu [a], Chang Chen [d], Jun Ke [e], Jacob C. Huang [d], Baojun Liu [a,*], Shaobin Wang [f,*]

[a] College of Resource and Environmental Engineering, Guizhou University, Guizhou Karst Environmental Ecosystems Observation and Research Station, Key Laboratory of Karst Georesources and Environment, Ministry of Education, Guiyang 550025, China
[b] Department of Environmental Engineering, Peking University, The Key Laboratory of Water and Sediment Sciences, Ministry of Education, Beijing 100871, China
[c] Department of Environmental and Chemical Engineering, Jiangsu University of Science and Technology, Zhenjiang 212003, China
[d] Department of Materials Science and Engineering, Hong Kong Institute for Advanced Study, City University of Hong Kong, Kowloon, Hong Kong
[e] School of Chemistry and Environmental Engineering, Wuhan Institute of Technology, Wuhan 430205, China
[f] School of Chemical Engineering and Advanced Materials, The University of Adelaide, Adelaide, SA 5005, Australia

## ARTICLE INFO

## ABSTRACT

Solar-driven conversion of nitrogen ($N_2$) into ammonia ($NH_3$) is a promising alternative to the Haber-Bosch process, while still suffers from low conversion efficiency due to inactive $N\equiv N$ bond. Herein, a novel pathway of photocatalytic air redox reaction (ARR) to ammonia via NO is proposed and tested over an effective catalyst of oxygen-vacancy-rich bimetallic Cu-Co organic framework ultrathin nanosheets ($O_{VR}$-CuCo-MOFs NS) under visible light. The catalyst with unique oxygen defective sites shows an excellent $NH_3$ synthesis rate from air ($287.76 \pm 7.02$ μmol $g^{-1} \cdot h^{-1}$), which is 5.4-fold higher than that from pure $N_2$. Moreover, experiments and theoretical calculations indicate that the transformation of air mainly follows a redox pathway, in which $N_2$ and $O_2$ can be trapped at the oxygen vacancies to generate nitric oxide (*NO) and further be reduced to ammonia by visible light. The ARR process shows a lower barrier of free energies in the onset activation step (*$N_2 \rightarrow$ *N-NO, $-0.08$ eV) and rate-limiting step (*NO $\rightarrow$ *NHO, 1.23 eV) compared with those of traditional nitrogen reduction (*$N_2 \rightarrow$ *N-NH, 1.48 eV and $H_2N$-$NH_2 \rightarrow$ *$NH_2$, 1.29 eV, respectively). This work provides a new and sustainable pathway for photo-driven ammonia synthesis.

## 1. Introduction

Ammonia ($NH_3$), a key intermediate in the global nitrogen cycle, plays a vital role in agricultural, biological, and industrial activities [1–3]. Currently, more than 90% of $NH_3$ production relies on the Haber-Bosch process, which is operated at high reaction temperature and pressure (300–500 ℃, 150–300 atm), leading to more than 1% of the global annual energy consumption and 1.6% of total global $CO_2$ emissions [4–6]. Photo-driven nitrogen reduction reaction (NRR) displays huge superiorities due to the mild reaction conditions, sustainability and low energy consumption [7–10]. Subsequently, many photocatalysts (e.g. $TiO_2$-based materials, carbon-based materials, and metal sulfides [11–19]) were developed and showed a good performance in $NH_3$ synthesis via traditional NRR. However, $NH_3$ production efficiency still suffers from two major issues in the conventional

photocatalytic NRR. Firstly, $N\equiv N$ bond in $N_2$ molecules is hard to be activated and cleaved due to the inherent four bonding orbitals ($\sigma_g 2p$) and four anti-bonding orbitals ($\pi_g$*2p) (triple bond energy: 941 kJ $mol^{-1}$). Additionally, the strong cleavage energy (410 kJ $mol^{-1}$) of the first bond in $N_2$ seriously hinders the process kinetics of $N_2$ hydrogenation. Hence, it is highly desirable to develop a novel pathway to break up the triple $N\equiv N$ bond with lower dissociation energy, and boost $N_2$-hydrogenation with a lower kinetic barrier.

Direct air redox reaction (ARR) in pure water is a potential way for photocatalytic $NH_3$ synthesis via coupled redox reactions. It is well known that the stable $N\equiv N$ bond in $N_2$ is easier to be broken up through an oxidation process with $O_2$ to form nitrogen oxides ($NO_x$), a natural occurring process by lighting, which exhibits a lower dynamic barrier than traditional NRR [20]. Liu et al. reported that ultrathin $WO_3$ nanosheets displayed an excellent performance (1.92 mg·$g^{-1} \cdot h^{-1}$) in

* Corresponding authors.
  E-mail addresses: jbliu@gzu.edu.cn (B. Liu), Shaobin.wang@adelaide.edu.au (S. Wang).

photocatalytic nitrate ($NO_3^-$) production under a gas mixture ($V_{N2}:V_{O2}$ =3:1) [20]. In addition, $NO_x$ reduction to $NH_3$ was also a more viable procedure with an 'up-hill' energy process [21,22], compared with the direct $N_2$-hydrogenation of NRR. Hirakawa et al. found that $TiO_2$ with surface defects exhibited a remarkable photo-transforming performance of $NO_3^-$ to $NH_4^+$ with high selectivity (97%) [21]. More importantly, Choi et al. demonstrated that nitric oxide could be more facile to be reduced to $NH_3$ rather than nitrate and nitrite anions over Bi/Carbon catalysts [22]. Accordingly, by coupling redox reactions, a novel pathway could be designed for photo-driven $NH_3$ synthesis through the direct ARR process via NO.

Metal-organic frameworks (MOFs) are intriguing platforms for photocatalytic processes with superiorities to carry out selective catalytic reactions by dexterous adjustments. Two-dimensional (2D) MOFs not only extend light response to the visible-light range and improve electron-hole separation, but also offer high specific surface areas (more active/reactive centers) with abundant defect sites for adsorption and activation of reactants [23–26]. Compared with single-metal MOFs, bimetallic nodes usually exhibit better thermal and water stability as well as an abundant structure variety. Although 2D materials can offer larger surface and enhance the migration of carriers, NRR needs more active sites for $N_2$ activation and hydrogenation in actual reaction processes. Currently, 2D materials developed by defect engineering (oxygen vacancies ($O_V$)) showed remarkable activity and selectivity in photocatalysis [27–31], especially beneficial for the activation and conversion of $N_2$ to $NH_3$ [32–35]. Therefore, constructing abundant $O_V$ on 2D photocatalysts via defect engineering is an effective way for photo-driven $NH_3$ synthesis.

Herein, ultrathin 2D CuCo-MOFs nanosheets (NS) with plentiful oxygen vacancies were fabricated (Fig. 1) and applied for $NH_3$ photosynthesis via coupled redox reactions of air (only $N_2$ and $O_2$) with water by visible light. The catalyst showed an excellent $NH_3$ generation efficiency of $287.76 \pm 7.02$ µmol g$^{-1}$·h$^{-1}$, which is 5.4-fold higher than that using pure $N_2$ ($51.94 \pm 3.61$ µmol/g·h). By designing the novel direct ARR process and $O_V$-rich catalysts, $N_2$ can be easily activated and cleaved on the $O_V$ sites, which are the key reaction centers for the photo-driven $NH_3$ synthesis. Furthermore, the onset and rate-limiting steps of the ARR process also show lower barriers than traditional NRR. This work puts forward a novel and sustainable pathway for $NH_3$ synthesis by defects engineered materials.

## 2. Experimental section

### 2.1. Synthesis of Cu-MOFs nanosheets

$Cu(NO_3)_2 \cdot 3H_2O$ (3.6 mg, 0.015 mmol), trifluoroacetic acid (1.0 M, 10 µL) and polyvinylpyrrolidone (PVP, average molecular weight = 40,000, 10.0 mg) in 12 mL of a mixture of dimethylformamide (DMF) and ethanol (V: V=3: 1) were put in a 20 mL capped vial. Then tetrakis (4-carboxyphenyl) porphyrin (TCPP, 4.0 mg, 0.005 mmol) in 4 mL of a mixture of DMF and ethanol (V: V=3: 1) was added dropwisely under stirring. After that, the solution was sonicated for 10 min. The vial was closed and heated to 80 °C for the reaction of 3 h. The resulting nanosheets were washed twice with ethanol and collected by centrifuging at 8000 r.p.m. for 10 min. Finally, the obtained Cu-MOFs nanosheets were redispersed in 10 mL of ethanol.

### 2.2. Synthesis of Co-MOFs nanosheets

$Co(NO_3)_2 \cdot 6H_2O$ (4.4 mg, 0.015 mmol), pyrazine (0.8 mg, 0.01 mmol) and PVP (20.0 mg) were dissolved in 12 mL of a mixture of DMF and ethanol (V: V=3: 1) in a 20 mL capped vial. Then TCPP (4.0 mg, 0.005 mmol) in 4 mL of a mixture of DMF and ethanol (V: V=3: 1) was added dropwisely under stirring. After that, the solution was sonicated for 10 min. The vial was closed and heated to 80 °C for the reaction of 24 h. The resulting red nanosheets were washed twice with ethanol and collected by centrifuging at 8000 r.p.m. for 10 min. Finally, the obtained Co-MOFs nanosheets were redispersed in 10 mL of ethanol.

### 2.3. Synthesis of CuCo-MOFs nanosheets

Solution A: $Cu(NO_3)_2 \cdot 3H_2O$ (3.6 mg, 0.015 mmol), trifluoroacetic acid (1.0 M, 10 µL) and PVP (30.0 mg) were dissolved in 24 mL of a mixture of DMF and ethanol (V: V=3: 1), then $Co(NO_3)_2 \cdot 6H_2O$ (4.4 mg, 0.015 mmol) and pyrazine (0.8 mg, 0.01 mmol) were put in the above solution and the mixture was put in a 30 mL capped vial. Solution B: TCPP (8.0 mg, 0.01 mmol) was added in 8 mL of a mixture of DMF and ethanol (V: V=3: 1). Subsequently, solution B was slowly injected to solution A under vigorous stirring. After further stirring for 20 min, the mixture was transferred into a 25 mL vial with a closed cap and heated in an oven at 80 °C for 24 h. The resulting red nanosheets were washed twice with ethanol and collected by centrifuging at 8000 r.p.m. for
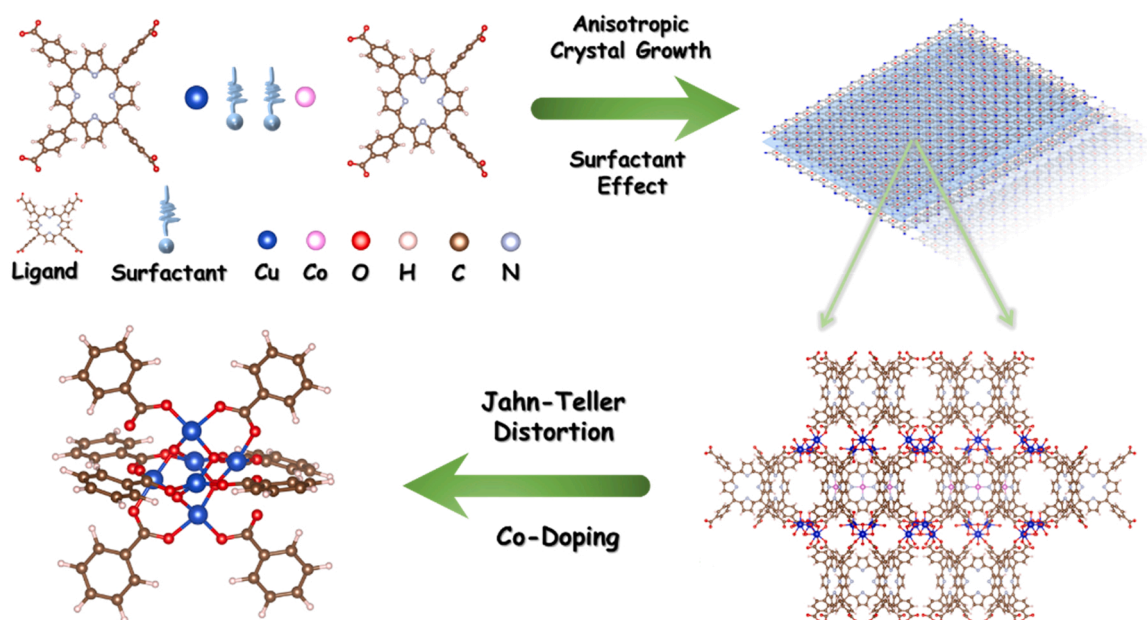


**Fig. 1.** Schematic illustration of the preparation process of $O_{VR}$-CuCo-MOFs NS.

10 min. Finally, the obtained CuCo-MOFs nanosheets were redispersed in 20 mL of ethanol.

## 2.4. Catalytic activity evaluation

The photocatalytic activities of the samples were evaluated under visible light irradiation ($\lambda \geq 400$ nm), using a 300 W Xe lamp (CEL-HXF300, China) as the light source. Reacted gases were pretreated by the process of acid, alkali and dry treating. A catalyst (5 mg) was dispersed in 100 mL of double distilled water by magnetic stirring, and then the dispersion was added to a quartz reactor. The reactor was equipped with a circulating water jacket in order to maintain temperature of 25 $^{\circ}$C. The catalyst suspension was continuously stirred in dark whilst high-purity $N_2$ ($N_2/O_2$) was bubbled through the suspension at a flow rate of 60 mL/min for 60 min to obtain a $N_2$ ($N_2/O_2$)-saturated aqueous suspension. Before the lamp was turned on, the suspension was continuously stirred for 30 min in dark to achieve adsorption-desorption equilibrium between the catalyst, dissolved $N_2$, $O_2$ and $H_2O$. The reactor was then irradiated using the 300 W Xe lamp. At regular intervals, 5 mL aliquots of the reaction solution were collected using a syringe, and then immediately centrifuged to remove the catalyst. The concentrations of $NH_3$ products were determined by colorimetry using the Nessler's reagent method and ions chromatography, respectively. UV-Vis absorption spectra of the colored complexes formed were recorded on a Shimadzu UV-2550 UV-Vis spectrometer, and the concentrations of $NH_3$ were determined using standard calibration curves of absorbance versus concentration.

## 2.5. Characterization of photocatalysts

The photocatalysts were characterized by X-ray diffraction (XRD), transmission electron microscopy (TEM), atomic force microscopy (AFM), electron spin resonance (ESR) spectroscopy, $N_2$ physisorption, UV-Vis spectroscopy, and photoelectrochemical tests. The details of these techniques were described in Supplementary Information.

## 3. Results and discussion

### 3.1. Mechanism of oxygen-vacancy-rich MOFs nanosheets

Ultrathin oxygen-vacancy-rich MOFs nanosheets ($O_{VR}$-CuCo-MOFs NS) with Cu and Co bimetallic nodes were synthesized (Fig. 1) by a surfactant polyvinylpyrrolidone (PVP) self-assembly strategy using metal ions and tetrakis(4-carboxyphenyl)porphyrin (TCPP). With the aid of the polyvinyl skeleton, a passivation layer could be created through the strong interaction among $Cu^{2+}$, $Co^{2+}$, and O atoms of the pyrrolidone ring. $Cu^{2+}$ as a divalent cation in the $O_{VR}$-CuCo-MOFs NS brings a strong Jahn-Teller effect for generation of defects [36–38]. In addition, the different coordination with two metallic nodes would bring in a disorder structure to create more oxygen defects over the $O_{VR}$-CuCo-MOFs NS, and the disorder would make the catalyst possess more thermodynamically stable structure [39–47]. Thus, an ultrathin MOFs nanosheet with bimetallic nodes and rich oxygen vacancies was obtained successfully. For comparison, ultrathin Cu-MOFs nanosheets with a little oxygen vacancies (named $O_V$-Cu-MOFs NS) and Co-MOFs nanosheets were also prepared.

### 3.2. Catalyst characterizations

Fig. S1a-b indicates clearly the layer structure of all MOFs NS by scanning electron microscopy (SEM). Additionally, the morphological feature was further studied by transmission electron microscopy (TEM) and high-resolution TEM (HRTEM). A plate structure can be seen, and the nearly transparent nature suggests the ultrathin character of the nanosheets (Fig. 2a and Fig. S1c). Furthermore, atomic force microscopy (AFM) determined the average thickness of the $O_{VR}$-CuCo-MOFs NS at 4–6 nm (Fig. S1d). Besides, Fig. 2b reveals Co and Cu nodes are uniformly distributed in the $O_{VR}$-CuCo-MOFs NS, indicating that the bimetallic MOFs NS was successfully synthesized. For more morphological information, the $O_{VR}$-CuCo-MOFs NS sample was further characterized by aberration-corrected scanning transmission electron microscopy (STEM) using the high-angle annular dark field imaging technique (Fig. 2c-e). A large amount of micropores and mesopores have been found on the $O_{VR}$-CuCo-MOFs NS (white circles with a red arrow),
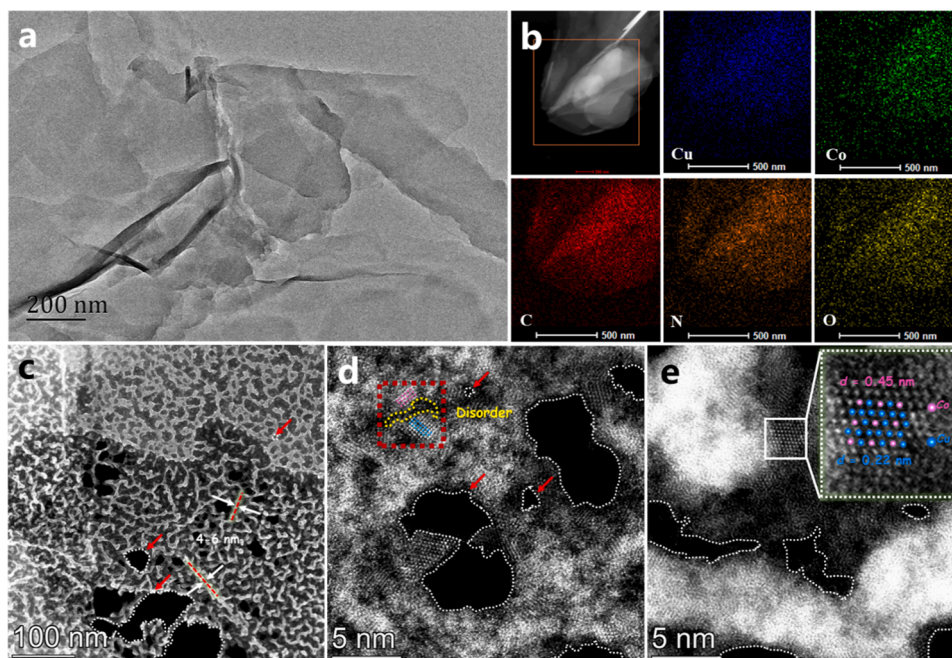


**Fig. 2.** (a) HRTEM; (b) Element mapping images of HRTEM; (c-e) Scanning transmission electron microscopy under the high-angle annular dark field (STEM-HADDF, Co: Pink ball, Cu: Blue ball) of $O_{VR}$-CuCo-MOFs NS.

which can also be derived from N$_2$ adsorption-desorption isotherms (Fig. S2a-**b**). In addition, as shown in Fig. 2**d**, some lattice disorders and dislocations could be observed on the surface of nanosheets (blue and red line, and yellow circle in red square), verifying rich vacancies on the nanosheet surface. Moreover, Fig. 2**e** shows the *d* space (0.22 nm) of Cu atom and 0.45 nm lattice distance of Co atom, and the points can illustrate their different atom distributions (Cu: blue ball, Co: pink ball) in the white square. The results indicated that lattice disorder and dislocation were formed on the surface of the O$_{VR}$-CuCo-MOFs NS due to O$_V$, which could supply the active sites for adsorption and activation of reactants [32–38].

X-ray diffraction (XRD) patterns of O$_{VR}$-CuCo-MOFs NS and O$_V$-Cu-MOFs NS are shown in Fig. 3**a**. Each sample displays the typical (002), (210), (004), and (110) Bragg reflections of Cu-TCPP, and the enhanced intensities of the (004) and (210) planes indicated the incorporation of cobalt dopants in the O$_{VR}$-CuCo-MOF NS. X-ray photoelectron spectroscopy (XPS) was applied to detect the bonding information and defect level (Fig. 3**b** and Fig. S3a-**b**). With Co introduction, the peaks of Co-N bond at ~ 779.5 and ~ 399.0 eV could be found in O$_{VR}$-CuCo-MOF NS (Fig. S3a-**b**). As shown in Fig. 3**b**, the Cu-O peak at ~ 933.6 eV shows a smaller intensity than that in O$_V$-Cu-MOFs NS, suggesting a higher oxygen defect level. O 1 s XPS spectra in Fig. S3c show that the O$_{VR}$-CuCo-MOFs exhibited a larger peak area of oxygen defects at ~530.5 eV than that in the O$_V$-Cu-MOFs NS, [36] indicating a higher concentration of O$_V$ in the O$_{VR}$-CuCo-MOFs NS. This phenomenon could be attributed to the outer sphere 3*d* orbit configuration of Co cations with three unpaired electrons, unlike the less unpaired 3*d* orbit of Cu cations, and the N atom could be captured by more unpaired electrons of Co. Accordingly, Co cations successfully combined with organic linkers in O$_{VR}$-CuCo-MOF NS. As shown in Fig. S3d, the two catalysts exhibit electron paramagnetic resonance (EPR) signals at g = 2.001, which is identified as the electrons trapped on oxygen defects. Notably, O$_{VR}$-CuCo-MOFs NS shows a higher EPR peak intensity than O$_V$-Cu-MOFs NS, proving more structural defects on the surface, which is consistent well with the reduced number of Cu-O coordination compared with O$_V$-Cu-MOFs NS (Fig. 3**e**). The results indicate Co doping induces compressive strain of the O$_{VR}$-CuCo-MOFs NS, thus leading to the lattice disorder and

dislocations and more vacancies. The high concentrations of O$_V$ in O$_{VR}$-CuCo-MOFs NS would accelerate catalytic reaction (Fig. 3**b** and Fig. S3b-**d**), since the O$_v$ is widely accepted to be the catalytic active site for solar-driven NH$_3$ production and Haber-Bosch process [15,16, 33–37].

X-ray absorption fine structure (XAFS) spectra were applied to investigate the local coordination of Cu species in O$_{VR}$-CuCo-MOFs and O$_V$-Cu-MOFs NS (Fig. 3**c-d**). X-ray absorption near-edge structure (XANS) provides sensitive information of the coordination symmetry of Cu. As shown in Fig. 3**c**, an obvious extra peak could be detected around 8977 eV due to doping of Co cations, indicating the introduction of coordination site disorder. The peak is different from that of O$_V$-Cu-MOFs NS and CuO at around 8980 eV. The result is consistent with the XRD and XPS characterizations. Besides, as shown in Fig. 3**d**, *k*-space spectra of Cu species in O$_{VR}$-CuCo-MOFs NS were not similar to those in O$_V$-Cu-MOFs NS and CuO, suggesting disorder coordination of Cu-O [37, 38]. More importantly, an obvious decrease of the K-edge oscillations could be found between 2 and 10 Å, which provided again the obvious variations of the coordination (at 5–10 Å) around the Cu atoms in O$_{VR}$-CuCo-MOFs and O$_V$-Cu-MOFs NS. The *R* space plots yielded three peaks of O$_V$-Cu-MOFs NS, corresponding to the Cu-N, Cu-O, and Cu-Cu metal shell at 1.0, 1.93, and 2.7 Å, respectively [36,48–54]. Compared with O$_V$-Cu-MOFs NS and CuO, O$_{VR}$-CuCo-MOFs NS showed only one peak of the Cu-O shell (Fig. 3**e**), and the intensity of the Cu-O shell peak gradually decreased and shifted to shorter distances [38,48]. The decreased peak intensity of Cu-O shell and reduced coordination numbers indicated a severe structural distortion of Cu species in O$_{VR}$-CuCo-MOFs NS. The observations are consistent with EPR and XPS results. The results strongly demonstrated that O$_{VR}$-CuCo-MOFs NS contained disorder structure and abundant O$_V$ species as shown in Fig. 3**f**. Moreover, as shown in Fig. S2c-**d**, temperature programmed desorption (TPD) under N$_2$ and O$_2$ atmosphere demonstrated more N$_2$ and O$_2$ desorption capacities and abundant O$_V$ species on the surface of O$_{VR}$-CuCo-MOFs NS [53-55].

The optical and electrical properties of the catalysts are vital factors for NH$_3$ generation. As indicated by UV–vis diffuse reflectance spectra (UV-DRS), the intrinsic absorption edges of O$_{VR}$-CuCo-MOFs and O$_V$-Cu-
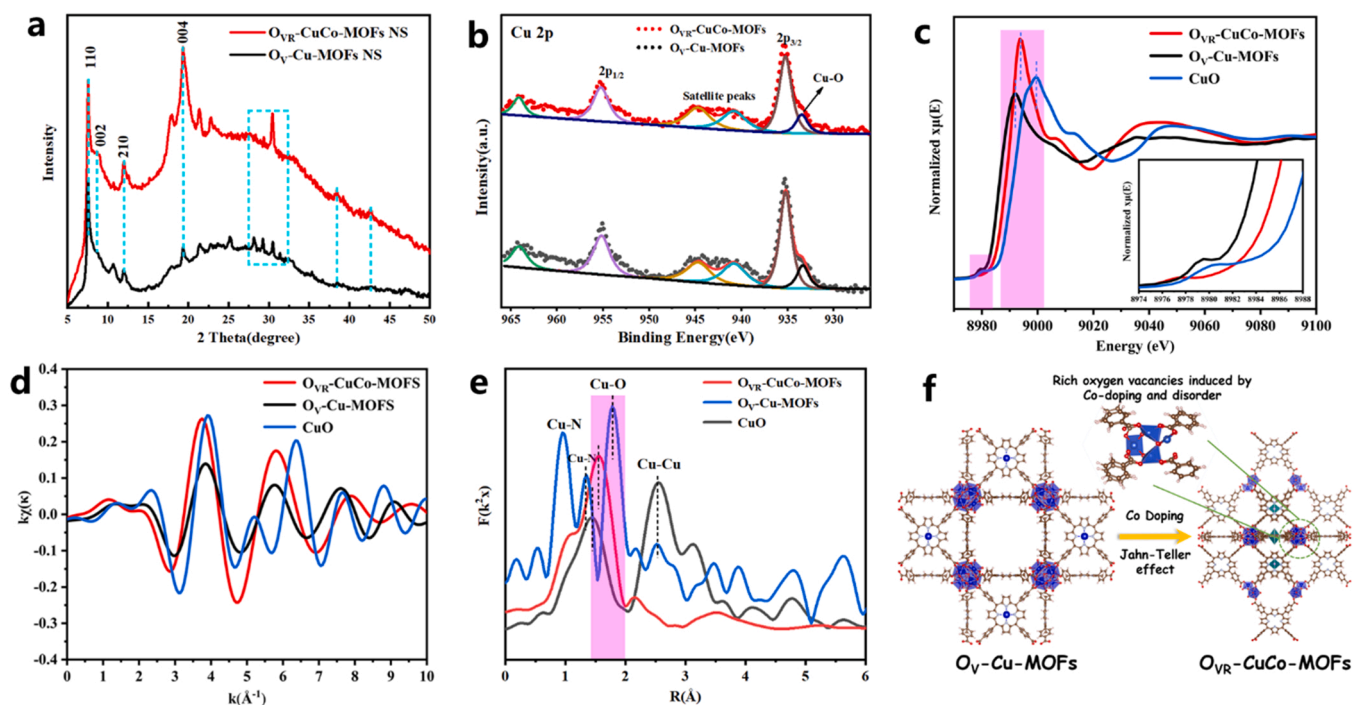


**Fig. 3.** (a) XRD patterns; (b) Cu 2p XPS spectra; (c) Cu XAFS; (d) Cu K-edge EXAFS oscillation functions $k^2\chi(k)$; and (e) R space spectra of extended X-ray absorption fine structure (EXAFS) of O$_{VR}$-CuCo-MOFs, O$_V$-Cu-MOFs NS and CuO; (f) Schematic of the oxygen vacancies and disorder in the as-synthesized O$_{VR}$-CuCo-MOFs NS.

MOFs were in analogic tendency (Fig. 4a). With regard to $O_{VR}$-CuCo-MOFs, $O_V$ and the synergistic effect between Cu and Co lead to strong absorption in the visible and near-infrared region. To investigate the separation and the lifetime of charge carriers, we adopted photo-luminescence (PL) and time-resolved photoluminescence decay (TRPD) spectroscopy, respectively. $O_{VR}$-CuCo-MOFs shows a weaker PL intensity than $O_V$-Cu-MOFs, indicating that the recombination of photo-induced carries is greatly impeded due to more $O_V$ (Fig. 4b). The $O_{VR}$-CuCo-MOFs NS also shows obviously longer average TRPL decay time ($\tau_1$=1.22 ns) than $O_V$-Cu-MOFs ($\tau_2$=0.91 ns) in Fig. 4c, which is well consistent with the PL results. An efficient photocatalytic activity depends on high quantum yields under light irradiation [32,35–38]. As shown in Fig. 4d, compared to $O_V$-Cu-MOFs, $O_{VR}$-CuCo-MOFs NS possesses higher apparent quantum yields (14.21%, $\lambda > 400$ nm) for the utilization efficiency of visible light, and more carriers can partake in NH$_3$ photosynthesis process [37,51]. Moreover, photo-electric current tests were further employed in a three-electrode system to estimate the superiority of charge transfer on MOFs NS. From Fig. 4e, $O_{VR}$-CuCo--MOFs NS exhibits 12-fold higher in current intensity than $O_V$-Cu-MOFs NS. Besides, from electrochemical impedance spectroscopy (EIS), $O_V$-Cu-MOFs displays a much bigger semicircle radius of Nyquist plots than $O_{VR}$-CuCo-MOFs NS, indicating the better charge transferability of $O_{VR}$-CuCo-MOFs NS mainly due to the high level of $O_V$ (Fig. 4f).

### 3.3. Photocatalytic air to ammonia on oxygen vacancies of $O_{VR}$-CuCo-MOFs NS

In evaluation of the performance of NH$_3$ formation ($\lambda > 400$ nm), $O_{VR}$-CuCo-MOFs NS and control samples were dispersed in pure water (Fig. S5a) and the produced NH$_3$ was detected using the Nessler's reagent and high-performance ion chromatography (HPIC, Fig. S4). As shown in Fig. 5a, $O_{VR}$-CuCo-MOFs NS exhibits varying ammonia generation performances with a following order: Ar (2.16 $\pm$ 0.61 μmol/g·h) < N$_2$ (51.94 $\pm$ 3.61 μmol/g·h) < N$_2$: O$_2$ = 4: 1 (118.65 $\pm$ 2.81 μmol/g·h) < Air (142.58 $\pm$ 1.99 μmol/g·h) < N$_2$: O$_2$ = 1: 1 (287.76 $\pm$ 7.02 μmol/g·h). Such results suggest that the redox process could enhance

NH$_3$ production, and the photocatalysts could not bring interference on the NH$_3$ yield as trace ammonium was found under Ar condition. This MOF catalyst displays a better performance of ammonia synthesis as compared to previously reported MOF-based materials (Supporting information, Table S1). A high concentration of oxygen could accelerate oxidation reaction to activate and break up N≡N, so more nitric oxide could be produced, and then reduced to NH$_3$. The best performance of NH$_3$ production is achieved under N$_2$: O$_2$ = 1: 1, with 85% selectivity of total photocatalytic reaction products, and the by-products of NO$_3^-$ and NO$_2^-$ could be detected by HPIC (Fig. S5b-c). To investigate the durability of $O_{VR}$-CuCo-MOFs NS, we carried out parallel and cycle experiments. The photocatalyst shows a similar performance with good quality, while it presents gradual deactivation due to the loss of active sites of oxygen defects in the photocatalytic ARR (Fig. 5b-c). However, the SEM images of the used nanosheets indicate that the structure remains the same as original morphology (Fig. S6). Moreover, the XPS characterizations show that the compositions and chemical states of the $O_{VR}$-CuCo-MOFs NS are not changed after the ARR reaction (Fig. S7).

In order to further track N$_2$ activation and hydrogenation processes that occurred on $O_V$ under air (N$_2$: O$_2$ =1: 1), we applied in situ Fourier transform infrared spectroscopy (FTIR) to monitor the surface intermediates formed during photocatalytic NH$_3$ synthesis (Fig. 5d-e). At the same time, in situ FTIR spectra on $O_{VR}$-CuCo-MOFs NS under CO$_2$ or Ar were also determined (Fig. S8). Due to the capture of N$_2$ on $O_V$, the signals of adsorbed species were observed (chemisorbed N$_2$ with the peak at 2350 cm$^{-1}$) [38]. The results are consistent with N$_2$-TPD, and rich oxygen vacancies would do a favor of gas adsorption (N$_2$ and O$_2$). The adsorbed H$_2$O can be seen at 3600–3000 and ~1648 cm$^{-1}$ (asymmetric stretching and bending modes, respectively). For key intermediates, two characteristic peaks (N-O bond at 875 and 1305 cm$^{-1}$) were obtained and visibly increased with the catalytic reaction time (Fig. 5d) [16,56]. The results indicate *NO, as the intermediate, would enhance the catalytic activity during the reaction process. Moreover, as shown in Fig. 5e, the peaks at 1558, 1648, and 1716 cm$^{-1}$ are referred to the antisymmetric and symmetric deformations of surface NH$_4^+$ species [37,57]. Similarly, the bands at 1268, 1607 and 1635, cm$^{-1}$ are
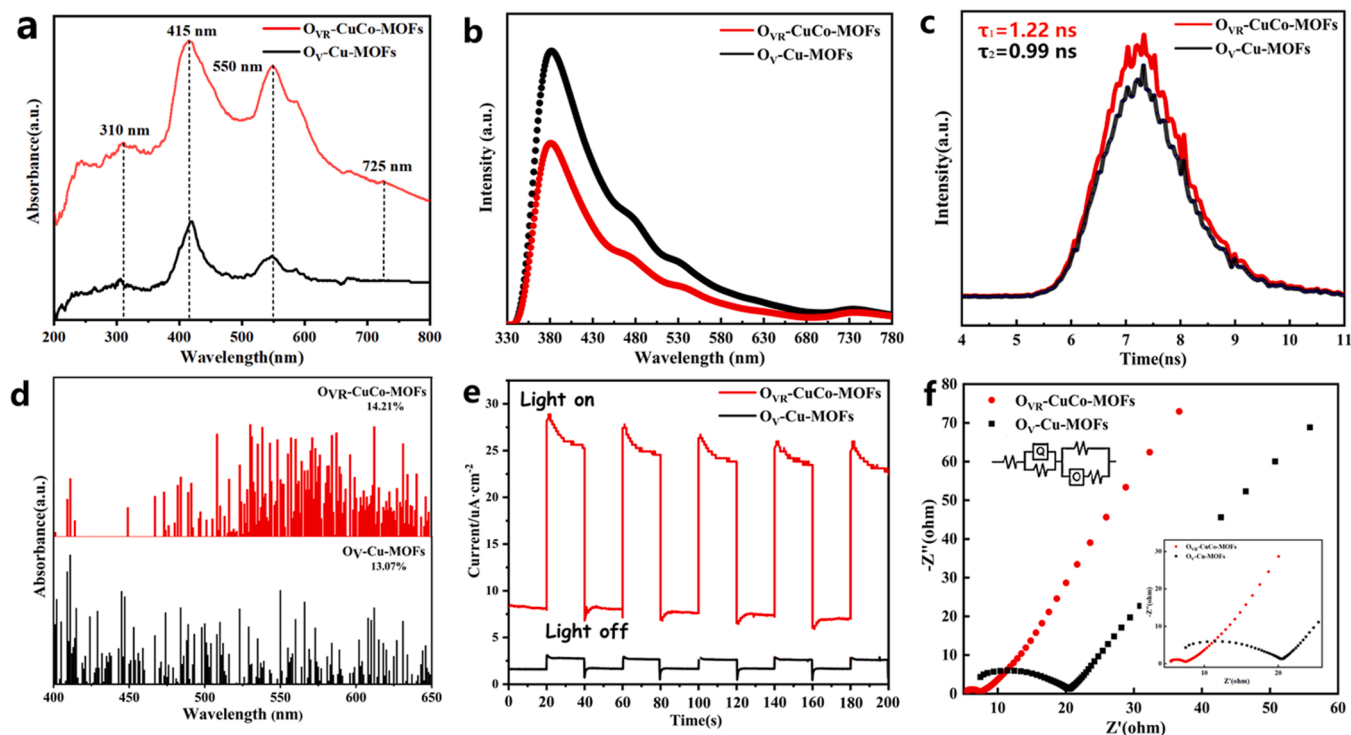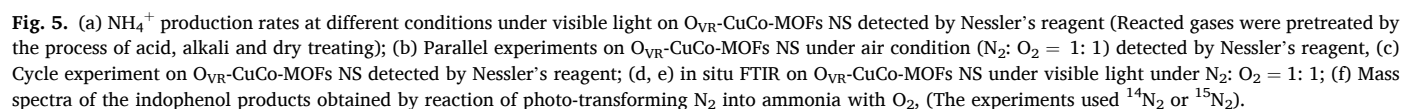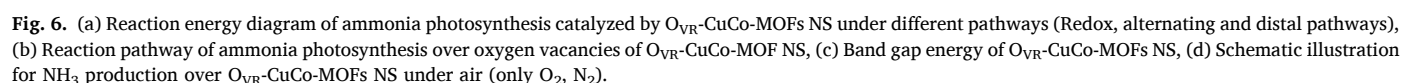


**Fig. 4.** (a) UV–vis DRS, (b) PL, (c) TRPD, (d) Apparent quantum yields under $\lambda > 400$ nm, (e) Photocurrent, (f) EIS of $O_{VR}$-CuCo-MOFs and $O_V$-Cu-MOFs NS.

**Fig. 5.** (a) $NH_4^+$ production rates at different conditions under visible light on $O_{VR}$-CuCo-MOFs NS detected by Nessler's reagent (Reacted gases were pretreated by the process of acid, alkali and dry treating); (b) Parallel experiments on $O_{VR}$-CuCo-MOFs NS under air condition ($N_2$: $O_2$ = 1: 1) detected by Nessler's reagent, (c) Cycle experiment on $O_{VR}$-CuCo-MOFs NS detected by Nessler's reagent; (d, e) in situ FTIR on $O_{VR}$-CuCo-MOFs NS under visible light under $N_2$: $O_2$ = 1: 1; (f) Mass spectra of the indophenol products obtained by reaction of photo-transforming $N_2$ into ammonia with $O_2$, (The experiments used $^{14}N_2$ or $^{15}N_2$).

σ(H-N-H) bending vibrations of $NH_3$ [50,57], and the peaks at 1055, 1099, and 1558 $cm^{-1}$ are σ(N-H) bending vibrations of $NH_3$ [38,58]. Those peaks give the important evidence of hydrogenation process,

indicating the novel catalytic reaction enhances the hydrogenation pathway. Besides, the absorption peaks at 3246 and 3555 $cm^{-1}$ represent the associated N-H stretching vibrations in the 3200–3600 $cm^{-1}$ region



**Fig. 6.** (a) Reaction energy diagram of ammonia photosynthesis catalyzed by $O_{VR}$-CuCo-MOFs NS under different pathways (Redox, alternating and distal pathways), (b) Reaction pathway of ammonia photosynthesis over oxygen vacancies of $O_{VR}$-CuCo-MOF NS, (c) Band gap energy of $O_{VR}$-CuCo-MOFs NS, (d) Schematic illustration for $NH_3$ production over $O_{VR}$-CuCo-MOFs NS under air (only $O_2$, $N_2$).

obscured by the presence of adsorbed water. For comparison, in situ FTIR was tested under Ar and $CO_2$ conditions, and the results indicate that rich $O_V$ would enhance $N_2$ adsorption and hydrogenation.

To confirm that the $NH_3$ originated from $N_2$ (rather than other external and interior interference), we carried out isotope labeling experiments ($^{15}N_2$ as a reactant). The $^{15}NH_4^+$ was quantified by the indophenol blue method [36,59,60], and further detected by liquid chromatography-mass spectrometry (LC-MS, Fig. 5**f**). After the catalytic reaction, the obtained solution revealed a strong mass spectroscopy peak at $m/z$ 199. Furthermore, the $^{15}N$: $^{14}N$ abundance ratio was higher when $^{15}N_2$, rather than $^{14}N_2$, was used as the source of nitrogen. Thus, the results indicated that the real source of ammonia is reactant nitrogen gas ($^{15}N_2$ and $^{14}N_2$), not the catalyst itself. Also, as for the source of oxidation reaction product ($NO_3^-$), high-efficiency mass spectrometry (HR-MS) was adopted to detect the resulting products, $^{15}NO_3^-$ and $^{14}NO_3^-$ (Fig. S5d), further confirming the ammonium from nitrogen gas.

*3.4. Reaction mechanism*

Theoretical calculations were then employed to investigate the possible reaction pathways (Fig. 6**a-b**) on oxygen vacancies of $O_{VR}$-CuCo-MOFs NS utilizing air ($N_2$: $O_2$ = 1: 1) by the Vienna Ab Initio Package (VASP). Combined with density functional theory (DFT) calculations, three pathways of ARR on oxygen vacancies were proposed and simulated under visible light irradiation (Fig. 6**a**). Pathway I: Nitrogen was oxidized to nitrogen oxide ($NO_x$) by coupling with oxygen, the oxidation reaction would keep going ($N_2 \rightarrow *NO \rightarrow *NO_2 \rightarrow NO_3$) on the surface of catalysts, and the reaction pathways and free energy were also calculated (Fig. S9). Then partial *NO was reduced and transformed into ammonia (Fig. 6**b** with a red arrow), some of which were detected by ion chromatography and in situ FTIR. Pathway II: Direct hydrogenation NRR process (Fig. 6**b** with black and blue arrows). Compared with the distal pathway, the alternating pathway displays a kinetic superiority of hydrogenation. As shown in Fig. 6**a**, the start-up step (*$N_2 \rightarrow$ *N-NO) of pathway I releases 0.04 eV of free energy (from −0.04 to −0.08 eV) comparing with *$N_2 \rightarrow$ *N-NH (from −0.04 to 1.48 eV) of the traditional NRR, indicating that the novel ARR has a kinetic superiority of spontaneity to break up and activate N≡N. Although the *NO → *NHO (from 1.02 to 1.23 eV) step exhibits the greatest energy barrier of pathway I, suggesting that this is the rate-determining step in $NH_3$ production, the remaining hydrogenation pathways have tended to spontaneously transform intermediates to $NH_3$ in general. The rate-determining step of traditional NRR is $H_2N-NH_2 \rightarrow$ *$NH_2$ with a barrier of 3.81 eV (from −2.52 to 1.29 eV). Thus, the novel ARR has an energy barrier of merely 0.21 eV (from 1.02 to 1.23 eV). More importantly, the lower energy barriers of $O_{VR}$-CuCo-MOFs NS in the final step of *$NH_2 \rightarrow$ *$NH_3$ (−6.84 eV) also possess priorities than traditional NRR (−4.83 eV). These results indicate fewer intermediates remain during the novel ARR for accelerating $NH_3$ synthesis. Therefore, $O_{VR}$-CuCo-MOFs NS shows much excellence in photo-transforming air ($N_2$ and $O_2$) into $NH_3$ via a redox process than direct hydrogenation process.

Generally, oxygen vacancies not only have many superiorities for $NH_3$ production but also can adjust the band energy structures [51,61]. In addition, the $O_V$-induced defect states act as the acceptor to inhibit the recombination of charge carriers [36–38,61], and also promote the interfacial charge transfer from the excited $O_{VR}$-CuCo-MOFs NS to activated $N_2$. Based on Tauc's equation, $O_{VR}$-CuCo-MOFs NS possesses a smaller bandgap (1.93 eV) than $O_V$-Cu-MOFs (2.03 eV) due to the presence of $O_V$, shown in Fig. 6**c** and Fig. S10a-**b**, and the positions of valence band and conduction band can also be seen (Fig. S10c-**d**). Meanwhile, the electronic energy-level diagrams of $O_{VR}$-CuCo-MOFs NS and $O_V$-Cu-MOFs NS are offered in Fig. S10d. Moreover, the possible mechanism of $NH_3$ synthesis (I: novel ARR and II: traditional NRR) over $O_{VR}$-CuCo-MOFs is provided in Fig. 6**d**. Especially, as proved by experimental and DFT results, more $NH_3$ synthesis is contributed to novel ARR than traditional process. Meanwhile, this redox reaction process could

break the conditional NRR kinetics barrier. Hence, this work successfully proves a novel $NH_3$ production route on $O_V$ sites that $N_2$ is oxidized by $O_2$ (cleaving N-N triple bond) and then *NO is transformed into $NH_3$ ($N_2$-hydrogenation). *NO, as the active intermediate, could remarkably improve the $N_2$ activation and hydrogenation to $NH_3$ synthesis.

## 4. Conclusion

In summary, an ultrathin $O_{VR}$-CuCo-MOFs nanosheet was successfully fabricated and applied in photocatalytic air redox reactions to $NH_3$ under visible light. The obtained $O_{VR}$-CuCo-MOFs nanosheets with rich oxygen vacancies exhibited a wide solar absorption range with enhanced charge carrier separation efficiency and superior performance of photo-transforming air into ammonia, achieving an ammonia production rate ($287.76 \pm 7.02$ μmol $g^{-1} \cdot h^{-1}$) by 5.4-fold higher than that with pure $N_2$. DFT calculations indicated that the transformation of air followed a novel redox pathway, in which $N_2$ and $O_2$ could be trapped at oxygen vacancies to generate nitric oxide (*NO) and further transform into ammonia. Compared with traditional nitrogen reduction reaction, the ARR process shows lower free energies of the onset activation step (*$N_2 \rightarrow$ *N-NO, from −0.04 to −0.08 eV) and rate-limiting step (*NO → *NHO, from 1.02 to 1.23 eV). This work provides a novel view for the development of effective photocatalysts with oxygen vacancies and strain engineering for photo-transforming air into ammonia.

## CRediT authorship contribution statement

**Wenjun Zhao**: Conceptualization, Methodology, Resources, Writing – original draft. **Qin Jiangzhou**: Software. **Wei Teng**: Validation. **Mu Jincheng**: Resources. **Chen Chang**: Visualization. **Jun Ke**: Formal analysis. **Jacob C. Huang**: Data curation. **Baojun Liu**: Resources, Funding acquisition, Supervision. **Shaobin Wang**: Writing – review & editing.

## Declaration of Competing Interest

The authors declare that they have no known competing financial interests or personal relationships that could have appeared to influence the work reported in this paper.

## Acknowledgements

## Appendix A. Supporting information

## References

[1] X.N. Zhang, B.B. Ward, D.M. Sigman, Global nitrogen cycle: critical enzymes, organisms, and processes for nitrogen budgets and dynamics, Chem. Rev. 120 (2020) 5308–5351.

[2] N. Gruber, J. Galloway, An earth-system perspective of the global nitrogen cycle, Nature 451 (2018) 293–296.

[3] C.K. Junium, A.J. Dickson, B.T. Uveges, Perturbation to the nitrogen cycle during rapid early eocene global warming, Nat. Commun. 9 (2018) 3186.

[4] K.A. Brown, D.F. Harris, M.B. Wilker, A. Rasmussen, N. Khadka, H. Hamby, S. Keable, G. Dukovic, J.W. Peters, L.C. Seefeldt, P.W. King, Light-driven dinitrogen reduction catalyzed by a CdS: nitrogenase MoFe protein biohybrid, Science 352 (2016) 448–450.

[5] G. Ertl, Reactions at surfaces: from atoms to complexity, Angew. Chem. Int. Ed. 47 (2008) 3524–3535.

[6] D. Zhu, L.H. Zhang, R.E. Ruther, R.J. Hamers, Photo-illuminated diamond as a solid-state source of solvated electrons in water for nitrogen reduction, Nat. Mater. 12 (2013) 836–841.

[7] P. Wang, F. Chang, W. Gao, J. Guo, G. Wu, T. He, P. Chen, Breaking scaling relations to achieve low-temperature ammonia synthesis through LiH-mediated nitrogen transfer and hydrogenation, Nat. Chem. 9 (2017) 64–70.

[8] C.J.M. Van der Ham, M.T.M. Koper, D.G.H. Hetterscheid, Challenges in reduction of dinitrogen by proton and electron transfer, Chem. Soc. Rev. 43 (2014) 5183–5191.

[9] I. Coric, B.Q. Mercado, E. Bill, D.J. Vinyard, P.L. Holland, Binding of dinitrogen to an iron-sulfur-carbon site, Nature 526 (2015) 96–99.

[10] S. Licht, B. Cui, B. Wang, F.F. Li, J. Lau, S. Liu, Ammonia synthesis by $N_2$ and steam electrolysis in molten hydroxide suspensions of nanoscale $Fe_2O_3$, Science 345 (2014) 637–640.

[11] S. Zhang, Y.X. Zhao, R. Shi, G.I.N. Waterhouse, T.R. Zhang, Photocatalytic ammonia synthesis: recent progress and future, EnergyChem 1 (2019), 100013.

[12] H.P. Jia, E.A. Quadrelli, Mechanistic aspects of dinitrogen cleavage and hydrogenation to produce ammonia in catalysis and organometallic chemistry: relevance of metal hydride bonds and dihydrogen, Chem. Soc. Rev. 43 (2014) 547–564.

[13] A.J. Medford, M.C. Hatzell, Photon-driven nitrogen fixation: current progress, thermodynamic considerations, and future outlook, ACS Catal. 7 (2017) 2624–2643.

[14] Z.X. Wei, Y.T. Zhu, J.Y. Liu, Z.C. Zhang, W.P. Hu, H. Xu, Y.Z. Feng, J.M. Ma, Recent advance in single-atom catalysis, Rare Met. 40 (2021) 767–789.

[15] G. Zhang, X. Yang, C. He, P. Zhang, H. Mi, Constructing a tunable defect structure in $TiO_2$ for photocatalytic nitrogen fixation, J. Mater. Chem. A 8 (2020) 334–341.

[16] H. Hirakawa, M. Hashimoto, Y. Shiraishi, T. Hirai, Photocatalytic conversion of nitrogen to ammonia with water on surface oxygen vacancies of titanium dioxide, J. Am. Chem. Soc. 139 (2017) 10929–10936.

[17] Y.Z. Chen, W.H. Li, L. Li, L.N. Wang, Progress in organic photocatalysts, Rare Met. 37 (2018) 1–12.

[18] J.Z. Qin, B.J. Liu, K.H. Lam, S.J. Song, X.Y. Li, X. Hu, 0D/2D MXene quantum dot/ Ni-MOF ultrathin nanosheets for the enhanced $N_2$ photoreduction, ACS Sustain. Chem. Eng. 8 (2020) 17791–17799.

[19] J.Z. Qin, X. Hu, X.Y. Li, Z.F. Yin, B.J. Liu, K.H. Lam, 0D/2D $AgInS_2$/MXene Z-scheme heterojunction nanosheets for improved ammonia photosynthesis of $N_2$, Nano Energy 61 (2019) 27–35.

[20] Y. Liu, M. Cheng, Z. He, B. Gu, C. Xiao, T. Zhou, Z. Guo, J. Liu, H. He, B. Ye, B. Pan, Y. Xie, Pothole-rich ultrathin $WO_3$ nanosheets that trigger N⎯N bond activation of nitrogen for direct nitrate photosynthesis, Angew. Chem. Int. Ed. 58 (2019) 731–735.

[21] H. Hirakawa, M. Hashimoto, Y. Shiraishi, T. Hirai, Selective nitrate-to-ammonia transformation on surface defects of titanium dioxide photocatalysts, ACS Catal. 7 (2017) 3713–3720.

[22] J. Choi, H.L. Du, C.K. Nguyen, B.H.R. Suryanto, A.N. Simonov, D.R. MacFarlane, Electroreduction of nitrates, nitrites, and gaseous nitrogen oxides: a potential source of ammonia in dinitrogen reduction studies, ACS Energy Lett. 5 (2020) 2095–2097.

[23] J. Di, J.X. Xia, H.M. Li, Z. Liu, Freestanding atomically-thin two-dimensional materials beyond graphene meeting photocatalysis: opportunities and challenges, Nano Energy 35 (2017) 79–91.

[24] L. Shi, Y. Yin, S.J. Wang, X.Y. Xu, H. Wu, J.Q. Zhang, S.B. Wang, H.Q. Sun, Rigorous and reliable operations for electrocatalytic nitrogen reduction, Appl. Catal. B 278 (2020), 119325.

[25] J. Di, J. Xiong, H.M. Li, Z. Liu, Ultrathin 2D photocatalysts: electronic-structure tailoring, hybridization, and applications, Adv. Mater. 30 (2018) 1704548.

[26] L. Shi, Y. Yin, S.B. Wang, H.Q. Sun, Rational catalyst design for $N_2$ fixation in ambient conditions: strategies towards enhanced conversion efficiency, ACS Catal. 10 (2020) 6870–6899.

[27] H. Li, C.L. Mao, H. Shang, Z.P. Yang, Z.H. Ai, L.H. Zhang, New opportunities for efficient $N_2$ fixation by nanosheet photocatalysts, Nanoscale 10 (2018) 15429–15435.

[28] S. Bai, N. Zhang, C. Gao, Y.J. Xiong, Defect engineering in photocatalytic materials, Nano Energy 53 (2018) 296–336.

[29] R. Shi, Y. Zhao, G.I.N. Waterhouse, S. Zhang, T.R. Zhang, Defect engineering in photocatalytic nitrogen fixation, ACS Catal. 9 (2019) 9739–9750.

[30] C. Mao, J. Wang, Y. Zou, H. Li, G. Zhan, J. Li, J. Zhao, L. Zhang, Anion (O, N, C and S) vacancies promoted photocatalytic nitrogen fixation, Green Chem. 21 (2019) 2852–2867.

[31] M. Cheng, C. Xiao, Y. Xie, Photocatalytic nitrogen fixation: the role of defects in photocatalysts, J. Mater. Chem. A 7 (2019) 19616–19633.

[32] W.J. Zhao, B.J. Liu, J.Z. Qin, J. Ke, L.L. Yu, X. Hu, Defect and interface engineering on two-dimensional nanosheets for photocatalytic $N_2$ reduction reaction, ChemphotoChem 4 (2020) 5233–5336.

[33] J. Humphreys, R. Lan, S.G. Chen, S.W. Tao, Improved stability and activity of Fe-based catalysts through strong metal support interactions due to extrinsic oxygen vacancies in $Ce_{0.8}Sm_{0.2}O_{2−δ}$ for the efficient synthesis of ammonia, J. Mater. Chem. A 8 (2020) 16676–16689.

[34] J. Humphreys, R. Lan, S.G. Chen, M. Walker, Y.S. Han, S.W. Tao, Cation doped cerium oxynitride with anion vacancies for Fe-based catalyst with improved activity and oxygenate tolerance for efficient synthesis of ammonia, Appl. Catal. B Environ. 285 (2021), 119843.

[35] X.P. Wu, L. Gagliardi, D.G. Truhlar, Cerium metal-organic framework for photocatalysis, J. Am. Chem. Soc. 140 (2018) 7904–7912.

[36] S. Zhang, Y. Zhao, R. Shi, C. Zhou, L.Z. Wu, Efficient photocatalytic nitrogen fixation over $Cu^{δ+}$-modified defective ZnAl-layered double hydroxide nanosheets, Adv. Energy Mater. 25 (2020), 1901973.

[37] Y.X. Zhao, R. Shi, L.Z. Wu, C.H. Tung, T. Zhang, Tuning oxygen vacancies in ultrathin $TiO_2$ nanosheets to boost photocatalytic nitrogen fixation up to 700 nm, Adv. Mater. 31 (2019), 1806482.

[38] Y.F. Zhao, Y.X. Zhao, L.Z. Wu, C.H. Tung, T. Zhang, Layered-double-hydroxide nanosheets as efficient visible-light-driven photocatalysts for dinitrogen fixation, Adv. Mater. 29 (2017), 1703828.

[39] R.D. Shannon, Revised Effective, Ionic radii and systematic studies of interatomic distances in halides and chalcogenides, Acta Crystallogr. Sect. A Found Crystallogr. 32 (1976) 925–945.

[40] X. Pan, M.Q. Yang, X. Fu, N. Zhang, Y.J. Xu, Defective $TiO_2$ with oxygen vacancies: synthesis, properties and photocatalytic applications, Nanoscale 5 (2013) 3601–3614.

[41] Q. Wu, Q. Zheng, R. Vande Krol, Creating oxygen vacancies as a novel strategy to form tetrahedrally coordinated $Ti^{4+}$ in $Fe/TiO_2$ nanoparticles, J. Phys. Chem. C 116 (2012) 7219–7226.

[42] G. Fan, F. Li, D.G. Evans, X. Duan, Catalytic applications of layered double hydroxides: recent advances and perspectives, Chem. Soc. Rev. 43 (2014) 7040–7066.

[43] Y. Sun, S. Gao, C. Lei, C. Xiao, Y. Xie, Ultrathin two-dimensional inorganic materials: new opportunities for solid state nanochemistry, Acc. Chem. Res. 48 (2015) 3–12.

[44] H. Li, J. Wu, Z. Yin, H. Zhang, Preparation and applications of mechanically exfoliated single-layer and multilayer $MoS_2$ and $WSe_2$ nanosheets, Acc. Chem. Res. 47 (2014) 1067–1075.

[45] V. Nicolosi, M. Chhowalla, M.G. Kanatzidis, M.S. Strano, J.N. Coleman, Liquid exfoliation of layered materials, Science 340 (2013) 1420.

[46] C. Tan, H. Zhang, Wet-chemical synthesis and applications of non-layer structured two-dimensional nanomaterials, Nat. Commun. 6 (2015) 7873.

[47] Y. Zhao, B. Li, Q. Wang, W. Gao, C.J. Wang, M. Wei, D.G. Evans, X. Duan, D. O'Hare, NiTi-layered double hydroxides nanosheets as efficient photocatalysts for oxygen evolution from water using visible light, Chem. Sci. 5 (2014) 951–958.

[48] Z. Jiang, W. Sun, H. Shang, W. Chen, T. Sun, H. Li, J. Dong, J. Zhou, Z. Li, Y. Wang, R. Cao, R. Sarangi, Z. Yang, D. Wang, J. Zhang, Y. Li, Atomic interface effect of a single atom copper catalyst for enhanced oxygen reduction reactions, Energy Environ. Sci. 12 (2019) 3508–3514.

[49] J. Zhang, Z.Y. Wang, W.X. Chen, Y. Xiong, W.C. Cheong, L.R. Zheng, W.S. Yan, L. Gu, C. Chen, Q. Peng, P. Hu, D.S. Wang, Y.D. Li, Tuning polarity of Cu-O bond in heterogeneous Cu catalyst to promote additive-free hydroboration of alkynes, Chem 6 (2020) 725–737.

[50] H. Shang, X. Zhou, J. Dong, A. Li, X. Zhao, Q. Liu, Y. Lin, J. Pei, Z. Li, Z. Jiang, D. Zhou, L. Zheng, Y. Wang, J. Zhou, Z. Yang, R. Cao, R. Sarangi, T. Sun, X. Yang, Engineering unsymmetrically coordinated $Cu-S_1N_3$ single atom sites with enhanced oxygen reduction activity, Nat. Commun. 11 (2020) 3049.

[51] H. Li, J. Shang, Z. Ai, L. Zhang, Efficient visible light nitrogen fixation with BiOBr nanosheets of oxygen vacancies on the exposed {001} facets, J. Am. Chem. Soc. 137 (2015) 6393–6399.

[52] J. Di, J. Xia, M.F. Chisholm, J. Zhong, C. Chen, X. Cao, F. Dong, Z. Chi, H. Chen, Y. X. Weng, J. Xiong, S.Z. Yang, H. Li, Z. Liu, S. Dai, Defect-tailoring mediated electron–hole separation in single-unit-cell $Bi_3O_4Br$ nanosheets for boosting photocatalytic hydrogen evolution and nitrogen fixation, Adv. Mater. 31 (2019), 1807576.

[53] B. Bai, H. Arandiyan, J. Li, Comparison of the performance for oxidation of formaldehyde on nano-$Co_3O_4$, 2D-$Co_3O_4$, and 3D $Co_3O_4$ catalysts, Appl. Catal. B Environ. 142–143 (2013) 677–683.

[54] J. Li, G. Lu, G. Wu, D. Mao, Y. Wang, Y. Guo, Promotional role of ceria on cobaltosic oxide catalyst for low-temperature CO oxidation, Catal. Sci. Technol. 2 (2012) 1865–1871.

[55] N. Sheppard, Vibrations of monatomic and diatomic ligands in metal clusters and complexes-analogies with vibrations of adsorbed species on metals. Vibrational Spectroscopy of Adsorbates, Springer, Berlin, Heidelberg, 1980, pp. 165–177.

[56] F. Giraud, C. Geantet, N. Guilhaume, S. Gros, L. Porcheron, M. Kanniche, D. Bianchi, Experimental microkinetic approach of De-$NO_x$ by $NH_3$ on $V_2O_5/WO_3/TiO_2$ catalysts. 1. Individual heats of adsorption of adsorbed $NH_3$ species on a sulfate-free $TiO_2$ support using adsorption isobars, J. Phys. Chem. C 118 (2014) 15664–15676.

[57] G. Ramis, M.A. Larrubia, An FT-IR study of the adsorption and oxidation of N-containing compounds over $Fe_2O_3/Al_2O_3$ SCR catalysts, J. Mol. Catal. A Chem. 215 (2004) 161–167.

[58] J.M.G. Amores, V.S. Escribano, G. Ramis, G. Busca, An FT-IR study of ammonia adsorption and oxidation over anatase-supported metal oxides, Appl. Catal. B Environ. 13 (1997) 45–58.

[59] L.R. Winter, B. Ashford, J. Hong, A.B. Murphy, J.G. Chen, Identifying surface reaction intermediates in plasma catalytic ammonia synthesis, ACS Catal. 10 (2020) 14763–14774.

[60] Y.X. Zhao, R. Shi, X.A. Bian, C. Zhou, Y.F. Zhao, S. Zhang, F. Wu, G.I. N. Waterhouse, L.Z. Wu, C.H. Tung, T.R. Zhang, Ammonia detection methods in photocatalytic and electrocatalytic experiments: how to improve the reliability of $NH_3$ production rates? Adv. Sci. 6 (2019), 1802109.

[61] S. Wang, X. Hai, X. Ding, K. Chang, Y. Xiang, X. Meng, Z. Yang, H. Chen, J. Ye, Light-switchable oxygen vacancies in ultrafine $Bi_5O_7Br$ nanotubes for boosting solar-driven nitrogen fixation in pure water, Adv. Mater. 29 (2017), 1701774.